1 # Seiche excitation in a highly stratified fjord of southern

2 # Chile: the Reloncaví fjord.

5 Manuel I. Castillo[1,2*], Oscar Pizarro[2,3,4] Nadin Ramírez[2,4] and Mario Cáceres[1]

8 [1]{Escuela de Biología Marina, Facultad de Ciencias del Mar y de Recursos Naturales,

9 Universidad de Valparaíso, Valparaíso, Chile.}.

10 [2] {COPAS-Sur Austral, Universidad de Concepción, Concepción, Chile.}

11 [3] {Departamento de Geofísica, Universidad de Concepción, Concepción, Chile.}

12 [4] {Instituto Milenio de Oceanografía, Universidad de Concepción, Chile.}

19 *Correspondence to: manuel.castillo@uv.cl

Abstract

We describe a seiche process based on current, temperature and sea level data obtained from the Reloncavi fjord (41.6° S, 72.5° W) in southern Chile. We combined four months of Acoustic Doppler Current Profiler (ADCP) data with sealevel, temperature and wind time series to analyze the dynamics of low-frequency (periods > 1 day) internal oscillations in the fjord. Additionally, seasonal CTD data from 19 along-fjord stations were used to characterize the seasonality of the density field. The density profiles were used to estimate the internal long-wave phase speed (c) using two approximations: (1) a simple reduced gravity model (RGM) and (2) a continuously stratified model (CSM). No major seasonal changes in c were observed using either approximation (e.g., the CSM yielded $0.73 < c < 0.87$ m s^{-1} for mode 1). The natural internal periods (T_N) were estimated using Merians's formula for a simple fjord-like basin and the above phase speeds. Estimated values of T_N varied between 2.9 and 3.5 days and were highly consistent with spectral peaks observed in the along-fjord currents and temperature time series. We conclude that these oscillations were forced by the wind stress, despite the moderate wind energy. Wind conditions at the end of winter gave us an excellent opportunity to explore the damping process. The observed damping time (T_d) was relatively long (T_d= 9.1 days).

1 Introduction

Internal seiche oscillation has long been known in closed basin geometries (e.g. Watson, 1904; Wedderburn, 1907; Wedderburn and Young, 1915). The first detailed description thereof was presented by Mortimer (1952). In these systems, wind is the main force affecting the surface and isotherms (Wiegand and Chamberlain, 1987), which produces a set of periodic oscillations and circulation cells throughout the water column that may contribute to internal mixing of the basin (Thorpe, 1974; Monismith, 1985; Wiegand and Chamberlain, 1987; Munnich et al., 1992; Mans et al., 2011; Simpson et al., 2011).

Although external (barotropic) seiches are ubiquitous in closed basin geometries (Münnich et al., 1992), it is not theoretically evident that there are internal seiches (baroclinic) in a linearly stratified fluid (Maas and Lam, 1995). It is possible to find resonant basin modes,

54 but only in well-behaved geometries (Arneborg and Liljebladh, 2001a). However, studies of

55 lakes have yielded good results using layered models (e.g. Lemmin, 1987), normal-mode

56 approximations (e.g. Wiegand and Chamberlain 1987; Münnich et al., 1992) or numerical

57 model simulations (e.g. Goudsmit et al., 2002). In fact, internal seiches have been observed

58 in semi-enclosed systems such as fjords (e.g. Djurfeldt, 1987; Pasmar and Stigebrandt, 1997;

59 Arneborg and Liljebladh, 2001a) with complex geometries and where linear stratification is

60 rarely observed, and thus the only way to maintain consistency with the theory is that the

61 oscillation in the pycnocline dominates the internal seiche oscillation (Arneborg and

62 Liljebladh, 2001a). Early in the development of a seiche, its amplitude is related to the

63 forcing intensity, and the standing oscillation then becomes free and requires no additional

64 forcing. The frequencies are retained, but the amplitude decays (damping) exponentially due

65 to friction until the system comes to rest (Rabinovich, 2010). The development of seiche

66 oscillations depends of the forcing and damping mechanisms; with large damping, it is

67 impossible to observe a seiche, whereas small damping of a seiche allows for several

68 oscillations (Arneborg and Liljebladh, 2001a).

69

70 In fjords with shallow sills, the interaction between the sill and the barotropic tide generates

71 internal tides that are more energetic than other internal oscillations and are the focus of most

72 studies regarding mixing and internal oscillations based on internal tides (e.g. Stigebrandt,

73 1980; Stigebrandt and Aure, 1989; Inall and Rippeth, 2002; Ross et al., 2014). In the case of

74 fjords with a deep sill and low tidal energy, the breaking of the internal seiche oscillations at

75 the boundaries could be an important contributor to the internal mixing, promoting the

76 spreading of properties within the fjord, particularly in deep waters (Stigebrandt and Aure,

77 1989; Münnich et al., 1992; Arneborg and Liljebladh, 2001b). Additionally, there are

78 evidences that vertical isopycnal displacements in fjords could be generated by similar

79 displacements outside the fjord (e.g. Svensen, 1980; Djurfeldt, 1987). These remotely

80 generated oscillations could enhance the mixing and ventilation in deep fjords.

81

82 There is still only limited understanding of the main oceanographic processes occurring in

83 the fjord region of southern Chile, although there has been local research during the previous

84 few decades. Since early studies of the hydrography by Pickard (1971), a systematic

85   measurement program in the fjord region has been maintained since 1995 (Palma and Silva,

86   2008; Pantoja et al., 2011; Iriarte et al., 2014), although only a small number of studies have

87   focused on the physical dynamics. Most studies have been conducted over short time spans

88   (e.g. Cáceres et al., 2004; Valle-Levinson et al., 2007), and only a few studies have been

89   based on more than one month of data (e.g. Valle-Levinson and Blanco, 2007; Letelier et al.,

90   2011; Castillo et al., 2012; Schneider et al., 2014), thereby limiting our understanding of sub-

91   inertial variability. In the Reloncavi fjord, time series of approximately 4 months have shown

92   evidence that 3-day oscillations of currents could be produced by internal seiche oscillations

93   (Castillo et al., 2012) but lack to describe the forcing mechanism and the seasonal

94   modulation.

95

96   This study presents the first evidence of internal seiche oscillations in a fjord in southern

97   Chile. The objective of this study was to address how these oscillations affect the temporal

98   and spatial dynamics of currents and temperature, and how these oscillations are forced

99

100   **2   Study area**

101

102   The Reloncavi fjord (41.5ºS, 72.5ºW) is the northernmost fjord on the coast of Chile (Fig. 1).

103   This "J" shaped fjord is 55 km long and has a width that varies from 3 km near the mouth to

104   1 km near the head. There is a deep sill (~ 200 m depth) located 15 km inland although it

105   does not appear to be a barrier to the exchange of properties between the adjacent basins.

106   Based on bathymetric features and the coastline morphology, this fjord can be separated into

107   four sub-basins displaying the characteristics presented in Table 1 and figure 2.

108

109   The main river discharge is provided by the Puelo River (at the middle of the fjord), which

110   produces a mean annual discharge of 650 m^3s^{-1}.The Petrohue River (at the head of the fjord)

111   has an mean annual discharge of 255 m^3s^{-1}, and there are additional freshwater inputs of

112   minor importance compared with the Cochamo river (mean annual discharge of 20 m^3s^{-1})

113   and Canutillar hydroelectrical plant (mean annual discharge 75.5 m^3s^{-1}) (Niemeyer and

114   Cereceda, 1984). The freshwater input to the fjord due to direct precipitation is only

115   approximately 2% of the main river discharge (León-Muñoz, 2013), and its contribution may

116   be in balance with evaporation (Castillo et al., 2016). The freshwater input creates a marked

117   along-fjord pycnocline that is deeper at the head (~8 m) and shallower at the mouth (~3 m)

118   (Fig. 2).

119

120   During the winter, the mean wind stress (τ) is low due to calms winds ($< 10^{-3}$ N m^{-2}). During

121   storm events in winter, τ can reach values as high as 0.4 N m^{-2} (winds of > 10 m s^{-1}), and the

122   wind tends to blow out of the fjord, thereby reinforcing the upper outflow of brackish water.

123   In contrast, during the spring/summer, the winds exhibit a marked diurnal cycle, and τ can

124   reach values as high as those observed in the winter, whereas the wind blows landward, i.e.,

125   toward the fjord's head and against the upper flow. Tides in the Reloncavi fjord are

126   predominantly semi-diurnal, and during spring tidal range never exceed 6 m, whereas the

127   neap tidal range is about 2 m. The tidal current is relatively weak in the upper layer, which is

128   dominated by gravitational circulation (Valle-Levinson et al., 2007; Montero et al., 2011;

129   Castillo et al., 2012).

130

131   **3   Data and Methods**

132
133   **3.1   Field Observations**
134

135   Current measurements were obtained using Teledyne RD Instruments ADCPs in three

136   subsurface mooring systems. These subsurface systems were located near the fjord mouth,

137   near the Puelo River and between the Cochamo and Petrohue Rivers (Fig. 1). The longest

138   time series spanned the period of August through November 2008 (Fig. 1 and Table 1). At

139   the mouth, two upward looking ADCPs were positioned at nominal depths of 10 m (300

140   kHz) and 450 m (75 kHz). The Puelo mooring held two ADCPs, one facing-up at a depth of

141   30 m (600 kHz) and one facing downward at a depth of 35 m (300 kHz). The Cochamo

142   mooring held one facing-up ADCP at a depth of 11 m (300 kHz). Note that due to the large

143   tidal range, the depths of the ADCPs significantly changed with the tides. These effects —

144   along with small vertical deviations of the ADCPs related to the line movements — were

145   corrected using the ADCPs pressure sensors, and all of the bin depths were referenced to the

146   water surface level. The mooring systems were designed to obtain the best vertical resolution

147   available with emphasis on the upper layer. The ADCP cell sizes were 0.5 m (600 kHz), 1 m

148 (300 kHz) and 4 m (75 kHz), and the data-acquisition time intervals were 10 minutes in most

149 of the ADCPs, with the exception of the deepest ADCP, which was set to acquire data at an

150 interval of 20 minutes. All the ADCPs configurations maintain a standard deviation< 2 cm s$^-$

151 ^{1} (details in supporting information S2).

152

153 The morphology of the fjord exhibits a sharp bend in the middle, and thus the x and y-

154 components of the currents were rotated to the local orientation of the along-fjord axis (Fig.

155 1 and Table 1). A right-handed coordinate system with a positive-up z-axis and an along-

156 fjord y-axis (positive toward the fjord head) was used. Consequently, the cross-fjord x-

157 component was positive toward the south (east) near the fjord mouth (head). To assess the

158 contribution of the tides to the currents, the amplitudes and phases of several tidal

159 components were calculated at all of the moored ADCPs using a standard harmonic analysis

160 from Pawlowicz et al. (2002).

161

162 The vertical structure of the temperature was obtained from Onset HOBO-U22 temperature

163 sensors installed in three mooring systems along the fjord (Fig. 1). These moorings held

164 surface buoys supporting the thermistor chains with an anchor located at a 25 m depth to

165 maintain their nominal depths (0, 1, 2, 3, 4, 5, 7, 9, 11, 13, 15 and 20 m) from the surface

166 independent of tidal fluctuations. Temperature data were collected every 10 minutes at all

167 locations.

168

169 A Davis Vantage Pro2 meteorological station was installed south of the Puelo River (see Fig.

170 1). This station held sensors for measuring the wind direction and velocity, solar radiation,

171 rain, and air temperature. The wind magnitude and direction sensors were installed 10 m

172 above sealevel and were set to collect data every 10 minutes from 12 June 2008 to 30 March

173 2011. Gaps in the time series represented only 0.04% of the total data. The wind stress (τ)

174 was calculated using a drag coefficient dependent on the magnitude (see Large and Pond,

175 1981) and a constant air density of 1.2 kgm^{-3}.

176

177 The salinity and temperature profiles were obtained seasonally using a CTD SeaBird SBE 25

178 at 19 stations in the along-fjord transect shown on Figure 1. The data were processed

179 following the standard protocol suggested by the manufacturer and were averaged in vertical

180 intervals of 0.5 m. Due to large salinity changes in the upper layer, the instrument pump was

181 set to a time interval of 1 minute. After the start of the pumping, the instrument was

182 maintained near the surface until the sensors stabilized. Then, the CTD was lowered to the

183 maximum depth of the station (Table 2). The along-fjord transects typically required 12 to 24

184 hours to complete, depending on local weather conditions. Due to technical limitations, the

185 winter transect was performed to a maximum depth of 50 m.

186

187 The sealevel was recorded every 10 minutes using two pressure sensors moored over the

188 seabed. At Cochamo, the pressure sensor was an Onset HOBO-U20, whereas a SeaBird

189 wave-tide gauge SBE-26 was installed near the fjord's mouth (Fig. 1). Subsurface pressure

190 data were corrected for air pressure and converted to an adjusted sealevel.

191

192 Discharge data were provided by Dirección General de Aguas, Chile (2016). These data are

193 regularly collected at a station located 12 km upstream of the Puelo River's mouth (Fig. 1).

194 The time series extended from January 2003 to December 2011, and data gaps represented

195 only 2% of the total.

196

197 **3.2   Time series analysis**
198

199 Previous findings (Castillo et al., 2012) have shown an important oscillation with a period of

200 approximately 3 days (72 h).To focus the study on these perturbations, the time series of

201 currents and temperature were band-pass filtered using a cosine-Lanczos with half

202 amplitudes at 60 h and 100 h (see results for the justification of the selected band). As part of

203 the results, the band-passed time series of the current (Fig. 6) and temperature (Fig. 9) data

204 are shown.

205

206 Spectral analyses of the current, wind stress, sealevel and temperature time series were

207 performed using Welch's modified average periodograms (Emery and Thomson, 1998). To

208 achieve statistical reliability of the spectral estimations, each time series was divided into

209 non-overlapping segments to generate spectral estimates. In the case of the current time

210 series, the spectra were (additionally) averaged among depth layers to obtain 12, 24 and 48

211 degrees of freedom, depending on the frequency (see Fig. 3). In addition, to evaluate the

212 consistency of the periodicity between the time series, we calculate a Morlet cross-wavelet

213 analysis following wavelet methods explained by (Torrence and Compo, 1998) and (Grinsted

214 et al., 2004).

215

216 The phase velocity (c) was estimated using two models that took into account the fjord

217 stratification: (1) a simple reduced-gravity model (RGM) and (2) a continuously stratified

218 model (CSM).

219

220 The reduced-gravity model was developed using the typical density profiles in each sub-

221 basin. Here, the base of the upper layer was estimated from the pycnocline depth (Fig. 2),

222 which in the Reloncaví fjord is well represented by the depth of the 24 isohaline (h_1)

223 (Castillo et al., 2016), considering that h_1 is the pycnocline depth and H is the deepest CTD

224 cast (mostly near to the sub-basins maximum depths). The mean density of the upper layer (

225 ρ_1) was estimated from depths between the surface to h_1, whereas the mean density for the

226 deep layer (ρ_2) was estimated for depths between h_1 and H. These estimations were made

227 for all sub-basins, and seasons (Table 2).

228

229 Using both densities, ρ_1 and ρ_2, the reduced gravity ($g' = g(\rho_2 - \rho_1)/\rho_2$) was obtained,

230 here g is the acceleration of gravity. The internal phase velocity of each sub-basin,

231 $c_i = \left(g' \ h_{1i} \right)^{1/2}$, where i =1 to 4 and h_{1i} represents the mean depth of the upper layer in the

232 sub-basin "i" was used to estimate the effective phase speed in the entire fjord (eq. 1) ,

$$c = L \sum_{i=1}^{n} \frac{c_i}{L_i} \tag{1}$$

233

234 where L_i is the i sub-basin length and L is the fjord length. This takes into account the

235 changes of depth and lengths of fjord's sub-basins. Similarly, the effective period (T) was

236 obtained by $T = c \ L^{-1}$.

237

238   The continuously stratified model (CSM) was developed using the normal mode analysis,

239   which introduced the stratification as $N^2 = -(g/\rho)(\partial\rho/\partial z)$, which is the buoyancy

240   frequency, in the Sturm-Liuoville expression

241
$$\frac{d}{dz}\left(\frac{1}{N^2}\frac{d\psi_n}{dz}\right)+\frac{1}{c_n^2}\psi_n=0 \qquad (2)$$

242   where $\psi_n(z)$ is the vertical structure of the horizontal velocity for the mode n. Here c_n

243   represents the n mode speed (see Gill, 1982) and differs significantly from phase speed if

244   rotation plays a role (van der Lee and Umlauf, 2011).

245

246   Independent of the model used to obtain the phase speed (RGM or CSM), the natural

247   oscillation period (T_N) was determined using Merian's formula for a semi-enclosed basin, as

248   suggested by Ravinovich (2010), $T_N = 4\,T$.

249

250   The modal decomposition was used to obtain the contribution of each mode in the currents

251   variability (e.g. Emery and Thomson, 1998; Gill, 1982; van der Lee and Umlauf, 2011). The

252   along- and cross-fjord band-pass currents [u_{bp}, v_{bp}] could be described by the vertical modes

253   by (3),

254
$$[u_{bp},v_{bp}](z,t)=\sum_{n=1}^{\infty}[u_{pj},v_{pj}](t)\;\psi_n(z) \qquad (3)$$

255

256   The along- and cross-fjord currents projected (u_{pj}, v_{bp}) on the vertical modal structure (ψ_n)
      was obtained by eq. (4),

257
$$[u_{pj},v_{pj}](t)=\frac{1}{H}\int_{-H}^{0}[u_{bp},v_{bp}](z,t)\;\psi_n(z)\;dz \qquad (4)$$

258

4. Results

4.1 Density structure

As a result of abundant freshwater input to the fjord, there were marked differences in density between the upper and lower layers along the fjord and small changes in stratification among seasons, particularly near the mouth of the fjord (Fig. 2). One important characteristic of the upper layer is its high and persistent stratification from the surface to the base of the pycnocline (Fig. 2). Along the fjord, the pycnocline depth exhibited clear deepening from 2.3 $\pm$ 0.1 m at the mouth to 6.1 $\pm$ 0.3 m near the head. The pycnocline depth exhibited greater seasonal variability near the head of the fjord (Fig. 2).

4.2 Winds, sealevel and freshwater discharge

The along-fjord wind stress (τ) displayed two patterns during the transition from winter to spring. During the winter, τ was generally directed out of the fjord (-0.4 $\pm$ 3 x10^{-2} N m^{-2}) and displayed oscillations with a period longer than 1 day. There were also strong events (> 0.2 N m^{-2}) during the first half of August 2008 that could be associated with the end of winter storms in the region. This winter pattern drastically changed during the early spring (first week of September 2008) and was maintained throughout the rest of the season. Changes were evident in a marked daily cycle and in switches from down- to up-fjord (average of 1.6 $\pm$ 3 x10^{-2} N m^{-2}), against the upper layer outflow (Fig. 3a).

The sealevel was measured at the mouth and near Cochamo (Fig. 1). At both stations, the form factor was 0.12, which indicates that semi-diurnal tides dominate in the region. In fact, the M_2 amplitude was 1.89 $\pm$ 0.06 m at the mouth and 1.91 $\pm$ 0.06 m near Cochamo. The mouth-to-head phase difference in this harmonic was negative (-2.4º), indicating propagation toward the head with a lag of approximately 5 minutes. The maximum tidal range during spring tides was approximately 6 m and less than 1 m during neap tides (Fig. 3b). Similar ranges have been observed outside the fjord in the Reloncavi sound (Aiken, 2008).

289   Discharge was greatest (approximately 1413 m^3 s^{-1}) at the end of August 2008 (winter) and

290   lowers (approximately 459 m^3 s^{-1}) at the end of October (spring). In the winter, the historical

291   mean of 650 m^3 s^{-1} (Niemeyer and Cereceda, 1984; Leon et al., 2013) was exceeded 86% of

292   the time, whereas during the spring, this exceedance occurred only 18% of the time. In fact,

293   only a small variability around the mean was observed during the spring (Fig. 3c).

294

295   **4.3   Along-fjord currents**

296

297   The along-fjord currents were one order of magnitude larger than the cross-fjord currents (in

298   this study we focused on the along-fjord component). At the three measurements sites at

299   Cochamo (Fig. 3d), Puelo (Fig. 3e) and the mouth (Fig. 3f), the along-fjord currents

300   displayed certain common features: (1) semi-diurnal oscillations attributed to tidal effect, (2)

301   a two layered structure with persistent outflow above the pycnocline and an intermittent

302   lower inflow layer beneath, and (3) several low-frequency (period > 1 day) oscillations were

303   present in the time series.

304

305   Currents in the upper outflow layer displayed a mean velocity of 66 cm s^{-1} at the mouth and

306   45 cm s^{-1} at Cochamo, indicating that the outflow increased through the mouth. Additionally,

307   the upper layer was deeper at Cochamo (Fig. 3d) than at the mouth (Fig. 3f), which is

308   consistent with the along-fjord pycnocline depth (Fig. 2). Below the upper layer, a sub-

309   surface layer displayed intermittent inflow (see Fig. 3d, 3e and 3f) with a maximum (> 20 cm

310   s^{-1}) centered at the ~ 6 m depth.

311

312   This two-layered pattern was clearly observed in the upper 10-15 m and is consistent with a

313   gravitational circulation due to the along-fjord pressure gradient. This pressure gradient is

314   also consistent with the observed along-fjord pycnocline tilt (Fig. 2). At depths > 20 m, the

315   along-fjord currents at Puelo and at the mouth exhibited an important influence (> 40% of

316   the variability) of a semi-diurnal component of the tide. In addition, in this layer, low-

317   frequency (periods > 7 days) oscillations suggest a bottom-to-surface propagation that was

318   more intense from the end of August to the beginning of September during a period of high

319   discharge (> 650 m^3 s^{-1}). This layer on average exhibited a weak outflow (~ 1 cm s^{-1}) at the

320   mouth, which in turn implies a 3-layer pattern of the residual flow near the mouth.

321

322   **4.4   Spectral characteristics of currents, temperature, sealevel and winds**

323

324   To obtain better statistic reliability, the spectra of the along-fjord currents were depth-

325   averaged. The upper layer was defined until the pycnocline depth ($z \leq h_1$), whereas the deep

326   layer contains $z > h_1$ (Fig. 4).

327

328   All of the spectra displayed an energetic peak at the semi-diurnal frequency (M$_2$), and this

329   peak was greater in the deep layer (Fig. 4). In the diurnal band, the spectra at Puelo and at the

330   mouth presented a clear (and highly energetic) peak in the surface layers. This diurnal peak

331   is likely due to the influence of wind stress (see Fig. S1), which displayed a marked diurnal

332   cycle during the late winter (end of August) and spring (Fig. 3a). An important peak (10^4 cm^2

333   s^{-2} cph^{-1}) was observed only at Cochamo in the 6 hour band (M$_4$), suggesting an increase in

334   the importance of non-linear interaction between M$_2$ and the bathymetry in this sub-basin.

335   The spectra in the upper layer displayed an important accumulation of energy in the band

336   centered on the 3days period. The band was wider (between 2 and 7 days) at the mouth and

337   Puelo and narrower (between 1.5 and 4 days) at Cochamo. At the mouth, the maximum

338   spectral density was in the 3 days band ($> 10^5$ cm^2 s^{-2} cph^{-1}) and was one order greater than

339   the maximum spectral density observed at Cochamo ($\sim 10^4$ cm^2 s^{-2} cph^{-1}). Another important

340   accumulation of energy in the along-fjord currents was centered on the 15 days period. One

341   characteristic of the 15 days band is the influence on the entire water column at Puelo and the

342   mouth (Fig. 4).

343

344   The sealevels at Cochamo (η_C) and at the mouth (η_m) were similar at frequencies less than

345   0.165 cph (periods longer than 6 h). The spectra displayed an important accumulation in the

346   synoptic band (10 days). Both locations exhibited the same energy at the diurnal (K$_1$)

347   semidiurnal (M$_2$) frequencies, although M$_2$ was clearly the dominant harmonic in the fjord.

348   The spectral energy was one order of magnitude higher than the diurnal (K$_1$) harmonics and

349   three orders of magnitude higher than the quarter-diurnal (M$_4$) harmonics. The spectra

350   exhibited no accumulation of energy in the 3days band, although at high frequencies (>0.5

351   cph), an important accumulation of energy was observed in the 1.3h band (between 1.16 h

352   and 1.56 h) at η_C (Fig. 4).

353

354   The wind stress (τ) indicated that the along-fjord wind stress was significantly higher than

355   the cross-fjord component. The spectra displayed a marked peak (particularly in the along-

356   fjord component) in the diurnal band, which is likely due to the sea-breeze phenomenon.

357   Another interesting feature of the spectrum was the peak in the semi-diurnal frequency,

358   which was observed in both components. At longer periods (>1day), the along-fjord wind

359   stress displayed an important but not statistically significant peak at 2.8 days, which is highly

360   consistent with the currents (Fig. 4).

361

362   **4.5   Seasonality of the internal oscillations**

363

364   The density structure on the fjord does not show an upper mixing layer along the seasons;

365   indeed a continuously stratified upper layer is present along the seasons (Fig. 5). The along-

366   fjord mean of the pycnocline depth (h_1), which was estimated based on salinity/density

367   gradient, was used to estimate the internal phase velocity (c) and the internal period (T_N).

368   Seasonally, h_1 does not change significantly during winter, spring and summer (between 4.6

369   and 4.8 m) but was shallower during autumn (~ 4.1 m) (Table 2).

370

371   In the case of the RGM approximation, internal phase velocities (c) were highest during

372   spring and summer (>0.83 m s^{-1}) whereas in winter and autumn the intensities were <0.76

373   m s^{-1}, thus we obtain internal periods between 2.9 and 3.4 days (70 and 82 hours) (Table 2).

374

375   The horizontal velocity structure (ψ_n) profile of the first 3 internal modes obtained from the

376   CSM showed high consistency along the fjord (in each sub-basin) and through the seasons

377   (Fig 5). The mode 1 was highly baroclinic, changing sign at nearly of 10 m (sub-basin I) and

378   15 m (sub-basin IV). In the case of mode 2 and 3, relatively high variability along the

379   seasons was observed specially at the sub-basins I and IV above of 20 m depth. For depths $>$

380   30 m (not shown in Fig. 5) the internal modes do not show significant variability (Fig. 5).

381   The modal speeds for the first 3 modes described above were relatively high during spring

382   and summer (c_1 was > 0.84 m s^{-1}) and lower during winter and autumn (here c_1 was < 0.77 m

383   s^{-1}). These results were highly consistent with the internal speeds obtained by RGM (Table

384   2).

385

386   Like the internal speeds (c), the natural internal period (T_N) obtained by RGM with the mode

387   1 of CSM were highly consistent. For comparison, we take into account T_N obtained from the

388   mode 1 of the CSM which ranged between 2.9 days (spring) and 3.5 days (winter). The

389   estimations of T_N with RGM showed speeds between 2.9 days (spring) and 3.4 days (winter

390   and autumn), indicating that oscillations between these periods are dominated by mode 1

391   internal seiche oscillation.

392

393   To focus on these internal seiche oscillations, we filtered the along-fjord currents with a 70h

394   to 90h cosine-Lanczos band-pass filter. Additionally, mode 1 of the internal seiche was

395   associated with the pycnocline depth, which is restricted to the upper 8 m (Fig. 2). Therefore,

396   we describe the along-fjord currents in the upper 10 m (Fig. 6).

397

398   The vertical pattern at the three locations shows inflow/outflow intermittence along the

399   whole time series; also most of these along-fjord structures seem to develop an inclination

400   which indicates the baroclinic nature of this pattern. The band-pass along-fjord currents were

401   intense at the mouth (> 15 cm s^{-1}) but diminish toward the head. Intense perturbations

402   oscillations were observed near the surface between 10 and 20 August 2008 at the mouth and

403   Cochamo, internal intensification (between 4 m and 10 m depth) of the inflow/outflow

404   pattern was clear at Puelo and Cochamo at the ends of September. To decide whether the

405   nature of the along-fjord currents pattern was baroclinic or barotropic we used $\psi_n(z)$ to

406   project the band-pass currents (eq. 3 and 4), similar to van der Lee and Umlauf (2011).

407

408   The agreement between the 3 days band-pass and the projected along-fjord currents at the

409   mouth is shown in Fig. 7. Using only the first three modes, it was possible to explain more

410   than 70% of the band-pass variability, changes in the outflow/inflow were highly consistent

411   and the intensifications at the surface were clearly shown by the projected modes. In

412   addition, the vertical structures of the outflow/inflow were well defined by the projections.

413   To make an approximation of the relative importance of the currents variability we estimated

414   kinetic energy ($K_E = (u^2 + v^2)/2$) of i) the projected modes 1-3, ii) the 3 days band-pass

415   and iii) the semi-diurnal (12h) + diurnal band pass (1d) along-fjord currents at the mouth.

416

417   The vertically averaged K_E obtained with 3 days band-pass was higher than that generated

418   with the other components (modes 1-3), the maximum was observed in the period 9 - 18

419   August (Fig. 7), which is consistent with the wind-stress intensification shown in Fig. 3a.

420   During that period, the modal K_E was about one third of the 3 days band-pass kinetic energy,

421   this ratio was higher (i. e. ca. 50%) during September. The importance of the tides at the

422   mouth was estimated by summing up the K_E of the diurnal and semi-diurnal currents. In

423   terms of energy, the K_E contribution of tides was similar to the modal currents (Fig. 7).

424

425   Along-currents were highly coherent at 3 days band which is the period of the first mode of

426   the internal seiche (Table 2). To describe the temporal variability of this high coherence,

427   along the time, we selected 3 m depth ADCP bins (on the upper layer) from the mouth, Puelo

428   and Cochamo to make a Morlet cross-wavelet analysis and to estimate the squared coherence

429   (only referred to as coherence hereafter) and phase spectra for the relations mouth/Puelo

430   (MP) (Fig. 8b, 8c) and Puelo/Cochamo (PC) (Fig. 8d, 8e). Both relations showed high

431   coherence in the semi-diurnal and diurnal band especially during spring-tides.

432

433   A low coherence (< 0.6) was observed during the down-fjord winds (Fig. 8a and 8b).

434   Similarly, the coherence for the PC relation was high along the 3 days band except during the

435   change of the wind direction described above (Fig. 8d). The associated phase spectra (only

436   the significant coherence) at the 3 days band was $\sim 0°$ indicating that the oscillation is in

437   phase along the fjord (Fig. 8c and 8e).

438

439   At the beginning of the time series, intense fluctuations were observed at Cochamo and at the

440   mouth (Fig. 6). To explore their relationship with the wind forcing, a detailed view of the

441   period between 8 and 31 August 2008, is presented in Fig. 9. During this period, the along-

442   fjord wind stress (not filtered) displayed three different states: (a) strong (> 0.2 N m^{-2}) up-

443   fjord winds, (b) weak (< 0.1 N m^{-2}) or nearly calm winds and (c) moderate ($\sim - 0.1$ N m^{-2})

444   down-fjord winds. During (c), the winds displayed an apparent diurnal cycle (e.g., Fig. 3a).

445

446   Although density is dominated by salinity, changes in the surface heat exchange may play a

447   seasonality role in the upper column. The rivers on the region are colder in winter producing

448   a clear thermal inversion (Castillo et al., 2016) while in summer the surface waters reach

449   18ºC by the heat gained by solar radiation. But the persistent pycnocline depth along the

450   seasons is consistent with the freshwater input suggesting that the variability of the density in

451   the upper layer is dominated by the freshwater input instead of the surface heating/cooling

452   variability. We used temperature moorings to emphasize that the internal oscillation reported

453   here had an expression in other properties of the water within the fjord. In addition, the band-

454   pass temperature time series and the along-fjord currents shows consistent oscillations

455   pattern (Fig. 9). During (a), the upper outflows weakened due to the opposing winds at the

456   surface. This change reached depths down to the pycnocline (Fig. 2), causing a disruption

457   and subsequently forcing of the internal oscillations observed in the currents and temperature

458   fields (Fig. 9). Here, intense perturbations were observed that weakened the surface outflow

459   and introduced the colder water of the upper layer to depths > 2 m at Cochamo and Puelo.

460   During (b), the upper outflow displayed minimum perturbations in both the currents and

461   temperature. In (c), perturbations in the currents and temperature were evident at Cochamo

462   and at the mouth with no major oscillations at Puelo (Fig. 9). In addition, 3 days band-pass

463   vertical velocities (w) were included as arrows on the contours of the along-fjord currents in

464   Fig. 9. The maximum w were 1 cm s^{-1} at the mouth, outflow (inflow) was related with

465   downward (upward) circulation in the entire fjord. This implies that the oscillation observed

466   on the along-fjord currents also was consistent with the vertical velocities patterns.

467

468

469   **5   Discussion**

470

471   We used data collected in one of the most extensive studies ever conducted in a Chilean

472   fjord. The data included currents (ADCPs) and temperatures from moored instruments,

473   seasonal CTD information and times series of winds and sealevel to study the dynamics of

474   the internal seiche oscillations in the Reloncavi fjord.

475

476   In fjords with shallow sills such as the Gullmar fjord in Sweden (Arneborg and Liljebladh,

477   2001a), the Knight Inlet in Canada (Farmer and Freeland, 1983) and the Aysen fjord in Chile

478   (Cáceres et al., 2002), internal tide oscillations may play major role in the internal mixing

479   (e.g. Stigebrandt, 1976; Farmer and Smith, 1980). In lakes, large internal seiche oscillations

480   significantly contribute to the mixing of the entire basin (Cossu and Wells, 2013), and these

481   oscillations could also be important in fjords where the relative importance of internal tides

482   may be less than the internal seiche oscillations (Arneborg and Liljebladh, 2001b). The semi-

483   diurnal signal in the spectra of the along-fjord currents (Fig. 4) suggests the relative

484   importance of internal tides on the region which is similar to other fjordal regions (e.g.

485   Stigebrandt, 1976; Allen and Simpson, 1998; Valle-Levinson et al., 2007). The tidal

486   interaction with the bathymetry is not the only mechanism to produce internal oscillations.

487   Recently Ross et al (2014, 2015) shows the forcing by glacier lake outburst floods (GLOFs)

488   and by low-frequency changes of barometric pressure. The relative importance of the

489   internal-tides on the southern Patagonian fjords is unknown and studies focused on

490   determine its contribution to the dynamics of currents and mixing must be done on future

491   studies.

492

493   In this study, we demonstrate the presence (and persistence) of seiches in a Chilean fjord

494   based on the sealevel slope (barotropic seiche), currents and temperatures (internal seiche).

495   We also studied the main processes forcing the natural oscillation of the pycnocline.

496

497   In the basic dynamic of a barotropic seiche into the fjord winds tilt the along-fjord surface

498   and piled water at the head of the fjord. The entire fjord basin begins to oscillate after the

499   wind stop. The maximum amplitude of the seiche is located at the head whereas a node (zero

500   amplitude) is located at the mouth of the fjord (Dyer, 1997; Rabinovich, 2010). In the

501   baroclinic seiche winds events which perturb the pycnocline to induce its oscillation in a

502   period accordingly with the fjord stratification (Djurfeldt, 1987). The horizontal structure of

503   currents associated with the seiche dynamics is related with the standing wave nature of the

504   seiche oscillation where the maximum currents occur in a node (the mouth) and minimum

505   currents are present in an anti-node (the head) in both closed and semi-closed basins (Dyer,

506   1997; Rabinovich, 2010).

507

508   At high frequencies, the tidal spectrum (Fig. 4) displayed a clear accumulation of energy

509   centered at a period of 1.3 h. This frequency is not related to any tidal harmonic interaction

510   (Pawlowicz et al., 2002), and the shape of the spectrum (not a peak) suggests resonance in

511   this frequency band. We explored the effect of the natural oscillation of the basin in this

512   pattern using the barotropic phase velocity (c) for a shallow water wave $c = (gh)^{1/2}$, where h

513   is the mean depth of the fjord. If one assumes a mean fjord depth of $h = 250$ m (Table 1),

514   then $c = 49.5$ m s^{-1}, and the natural period $T_N = 4L\,c^{-1} = 1.24$ h. This period is lower than the

515   observed period in Fig. 5 (1.3 h) because the mean depth takes into account the entire fjord

516   bottom profile (Fig. 1), and thus the effective depth (up to Cochamo) was 233 m and it is

517   closer to the 226 m necessary to obtain the observed period in Fig. 5. Winds in the region are

518   moderate (see Fig. 3), but their intensity is sufficient to tilt the surface slope at Cochamo

519   (Castillo et al., 2012), and thus the surface of the fjord oscillates with the natural period of

520   the basin. Further evidence of this pattern is provided by the clear differences in amplitude of

521   the sealevel spectrum at Cochamo (near the fjord's head) and at the mouth. This association

522   is attributed to the dynamics of seiches in fjords, which tend to produce a node at the mouth

523   and an anti-node at the head (Dyer, 1997). At the node, the sealevel amplitude must be zero,

524   whereas near the head, it must be a maximum. This pattern is highly consistent with the

525   observed spectra at 1.3 h (Fig. 5). Based on all of these results, we suggest that oscillations

526   close to 1.3 h will resonate with the natural period along the fjord.

527

528   Daily winds were highly coherent with surface along-fjord currents, especially on the

529   brackish water layer (S1). During the spring, daily periodicity of winds was strong (Castillo

530   et al., 2016) with intensities capable of perturbing the pycnocline and to induce the internal

531   seiching process.

532

533   The surface slope indicates that the sealevel at Cochamo was 0.07 m higher than at the

534   mouth, and this value can be taken as the amplitude of the surface seiche. According to the

535   RGM, the pycnocline deviation (η_1) is related to the surface elevation (η_0) in the form

536    $\eta_1 = -(\rho/\Delta\rho)\ \eta_0$, which implies that for a mean surface perturbation of 0.07 m and a typical

537    $\Delta\rho$ of 15 kg m^{-3}, we obtain a mean η_1 of -4.8 m. This finding indicates that the water piles

538   up at the head of the fjord, likely due to the predominant into the fjord winds in the region

539   (Fig. 3a) and produces a pycnocline deepening of about 5 m (Fig. 2).

540

541   At low frequencies (periods > 1 day), the along-fjord currents spectra displayed a marked

542   peak in energy centered at 3 days. To explore the origin of this variability, we analyzed the

543   density profiles along the fjord (Fig. 2) and applied two methods, the RGM and CSM. The

544   internal phase velocities (*c*) obtained from both methods were similar, and ranged between

545   0.73 m s^{-1} and 0.87 m s^{-1} (taking into account the mode 1 of CSM for comparison). The high

546   *c* value was obtained during the spring (November 2008), when the upper layer presented the

547   lowest densities of the seasons, likely due to high discharge (> 1000 m^3 s^{-1}). Remarkably, the

548   stratification is linked to the freshwater input despite no major observed changes in *c* (Fig.

549   6e-h). The high consistency between the CSM (mode 1) modal speeds and the phase speed

550   obtained by RGM suggest that rotation do not play a significant role on the along-fjord

551   dynamics of these oscillations (van der Lee and Umlauf, 2011). But cross-fjord, the

552   dynamics has been nearly geostrophic, especially at the fjord's mouth (Castillo et al., 2012).

553

554   For longer periods (> 10 days), there are evidences of baroclinic oscillations clearly observed

555   on the along-fjord time series (Fig. 3) and in the averaged spectra (Fig. 4). Recently, Ross et

556   al., (2015), described a similar periodicity on currents of a southern Patagonian fjord of Chile

557   associated to Baroclinic Annular variability, a regional feature on the air-pressure in the

558   region. This mechanism of generation for the 10 days oscillations on the Reloncavi fjord

559   needs to be verified on future studies.

560

561   The internal T_N of the entire fjord displayed periods between 2.9 and 3.5 days. These results

562   suggest that the accumulation of energy observed in the along-fjord currents are due to the

563   first mode of an internal seiche oscillation in the fjord. This result could be explained by the

564   presence of a node at the mouth, where the sealevel amplitude is minimum (Fig. 5) but the

565   currents are maxima (Figs. 3 and 6). This difference was also observed in the projected

566   currents (u_{pj}, v_{pj}) supporting the idea of the presence stationary wave along the fjord.

567   Additionally, the currents were highly coherent and in phase (Fig. 8) as we expected from a

568   basin-scale seiche wave like. As a way to estimate the contribution of the internal seiche to

569   the internal mixing the K_E was enhanced during the into the fjord winds (Figs. 3 and 7),

570   which were periods when the internal seiche band (3 days) was highly coherent along the

571   fjord (Fig. 8).

572

573   The winds exhibited high coherence with the along-fjord currents until the pycnocline

574   depths, at frequencies centered at 1 and 3 days (see Fig. S1). To study the extent to which the

575   wind stress perturbs the pycnocline, we used the Wedderburn number, which is given by the

576   equation $W = (h_1 / L)Ri$ (Thompson and Imberger, 1980; Monismith, 1986), where

577   $Ri = g\,'(h_1 / u_*^2)$ represents the bulk Richardson number, an index of the stability of the upper

578   layer (h_1). The frictional velocity (u_*) is obtained from the surface wind stress using the

579   equation $u_*^2 = \tau / \rho_0$, which results in the equation,

$$W = \frac{h_1^2 \varDelta\rho g}{L\tau} \tag{5}$$

581

582   According to Thompson and Imberger (1980), this value indicates the effect of the wind

583   stress on local upwelling in a stratified fluid (i.e., perturbing the pycnocline). Under weak τ

584   conditions ($W \gg 1$), the wind energy is insufficient to tilt the interface. Under strong τ

585   conditions ($W \ll 1$), however, upwelling conditions dominate, there by tilting the interface,

586   which produces conditions favorable to forcing of the internal seiche. The critical conditions

587   ($W \sim 1$) indicate the beginning of upwelling (Thompson and Imberger, 1980; Stevens and

588   Imberger, 1996), although the ideal transition point occurs at $W = 0.5$ (Monismith, 1986). All

589   of these conditions were observed during the period of August 2008, as it is shown on Fig. 9.

590   During strong τ ($\sim$0.3 N m^{-2}) conditions, $W = 0.27$ produced intense perturbation of the

591   pycnocline (Fig. 9a). In contrast, during weak τ ($\sim$0.01 N m^{-2}) conditions, a value of $W = 8$

592   indicates that the wind was too weak to perturb the pycnocline, favoring a seiche damping

593   process (Fig. 9b). Transition conditions occurred when $\tau \sim 0.1$ N m^{-2} and $W = 0.8$, indicating

594   that the winds were strong enough to perturb the pycnocline and stop the damping process

595   (Fig. 9c).

596

5.1   Internal seiche damping

598

599   The wind stress changed from a state where τ was strong enough to actively disturb the

600   pycnocline ($W < 1$) to a period of nearly calm winds ($W > 1$) between the 16 and 24 August

601   2008 (Fig. 9). During this period, both the along-fjord currents and temperatures tended to

602   decay, which is clearly evident in the isolines of these properties at the three sites (Fig. 9).

603

604   To study the damping process in detail, we selected the time series of the along-fjord

605   currents at a depth of 3 m at Cochamo during the above period in August to span the period

606   of forcing, damping and re-enforcing of the internal oscillation.

607

608   Typically, any real oscillations undergo damping, which is given by the equation,

609    $$x(t) = A\ e^{(-k\ t)} \cos(\omega\ t + \phi) \qquad (7)$$

610   where t is time and A is the initial amplitude, k is the damping coefficient which has units of

611   [s^{-1}], $\omega = 2\pi/T_N$ and ϕ is the phase. In the case studied here, $\phi = 0$, $A = 8$ cms^{-1}, and $T_N = 2.5$

612   days, which was the internal period at Cochamo (Fig. 4). The best fit occurred when $k = 1/3$

613   (Fig. 10).

614

615   The time for the initial amplitude A to decay to $A{\sim}0$ is the damping time (T_d). There was a

616   good fit (Fig. 10) between the observed current and the curve adjusted with the damping

617   effect. Here, $T_d = 9.1$ days, which is more than 3 times longer than the natural oscillation

618   (T_N); more precisely, $T_d = 3.6\ T_N$ at this site. The observed internal oscillations of the

619   currents were not completely damped because the winds increased from nearly calm ($W > 1$)

620   to moderate conditions, which disturbed the pycnocline ($W{\sim}1$) and induced the intense

621   oscillations during the spring (Fig. 6). In the spring, the winds displayed a marked diurnal

622   cycle that remained during the spring and summer (Castillo et al., 2012). This finding

623   suggests that the internal seiche (mode 1) process is active without damping because it is

624   forced daily (Fig. 3). Our findings indicated that the internal seiche process is an active

625   contributor for the mixing in the Reloncavi fjord, the magnitude of this contribution might be

626   similar as the tidal forcing. The maximum amplitude of the tidal currents on the Reloncavi

627   fjord is 10 cm s^{-1} (Valle-Levinson et al., 2007; Castillo et al., 2012), using the K_E to estimate

628   the maximum contribution of the tide obtain 5 x 10^{-3} m^2 s^{-2} which is similar to the observed

629   K_E at the mouth (Fig. 7). One example of the dissipation of the energy through this process

630   was observed previous to 19 August 2008 (Fig. 10), then the maximum currents were 0.7 m

631   s^{-1} and through eq. 7, we obtain K_E= 7 x 10^{-3} m^2 s^{-2}, meaning that a great part of this energy

632   might be dissipated within the Reloncavi fjord on 9 days.

633

634   **6   Conclusions**

635

636   The along-fjord seasonal density structure of the Reloncavi fjord showed small changes in

637   the stratification. The upper layer shows a persistent stratification from the surface to the

638   pycnocline base, the latter of which has a mean depth of 2 m near the mouth and 6 m near the

639   head of the fjord.

640

641   The along-fjord sealevel signal showed a 1.3 h energetic peak not related with any tidal

642   harmonics, additionally at this period the sealevel amplitude at the mouth was significantly

643   higher than the sealevel at the head of the fjord. This pattern was consistent with the presence

644   of a barotropic seiche on the Reloncavi fjord.

645

646   Local winds stress was able to perturb the along-fjord pycnocline and produce internal seiche

647   oscillations. The period centered on 3 days was consistent with the first baroclinic oscillation

648   mode. This mode explained 44% of the variability of the 3 days band. The oscillation was

649   highly coherent along the fjord and with a phase close to 0º, consistent with a standing wave,

650   like an internal seiche, within the Reloncavi fjord.

651

652   The internal seiche could be strong contributor to the internal mixing within the fjord, in fact

653   the kinetic energy (K_E) associated to the internal seiche was similar to the maximum

654   contribution of the tides in the along-fjord currents. During winter, the internal oscillations

655 were present a relatively long period of time with nearly calm winds, which permitted the

656 estimation of the damping time of the internal seiche being 9 days, otherwise during the

657 spring daily winds continuously forced the pycnocline.

658

659 Future studies should focus on evaluating more precisely the available energy for the mixing

660 process within the fjord and their effects on other water properties such as the salinity,

661 oxygen or nutrients.

662

663

664 **Data availability**

665

666 The installation of the moorings for measuring the current, temperature and sealevel in the

667 region was approved by the Chilean Navy through permit DS711. No specific permits were

668 required to install the meteorological station because the location is a publicly controlled site.

669 This study also did not involve any endangerment to species in the region. The authors

670 indicated that all data are available to download from a COPAS-SUR Austral (2012) website

671 (http://www. reloncavi.udec.cl/, last access 6 June 2016).The discharge data from the rivers

672 of Chile are available from the Dirección General del Aguas de Chile website

673 (http://dgasatel.mop.cl/, last access 1 July 2016). Also, all data sets can be requested from the

674 corresponding author (Manuel I. Castillo).

675

676 **Acknowledgements**

677 The authors thank the students (from Chile and Sweden) and technicians of the Physical

678 Oceanography group of the Universidad de Concepcion who collaborated in performing the

679 field measurements. This study is part of the COPAS-Sur Austral CONICYT PIA PFB31

680 and Centro de Investigación en Ecosistemas de la Patagonia by FIP2007-21. Manuel I.

681 Castillo was supported by CONICYT-PAI no. 791220005 and by FONDECYT no.

682 11160500. Finally, we want to thank the three anonymous reviewers and to the editor Mario

683 Hoppema for their comments which helped to improve the present manuscript.

684

685

References

Allen, G.L., and Simpson, J.H: Reflection of the internal tide in Upper Loch Linnhe, a
    Scottish fjord. Estuarine Coastal and Shelf Science 46, 683-701, 1998.

Arneborg, L., and B. Liljebladh.: The internal seiches in Gullmar fjord part I -dynamics.
    Journal of Physical Oceanography **31:** 2549-2566, 2001a.

Arneborg, L., and B. Liljebladh: The internal seiches in Gullmar fjord part II - contribution
    to basin water mixing. Journal of Physical Oceanography **31:** 2567-2574, 2001b.

Cáceres, M., A. Valle-Levinson, H. Sepúlveda, and K. Holderied: Transverse variability of
    flow and density in a Chilean fjord. Continental Shelf Research **22:** 1683–1698,
    2002.

Castillo, M. I., O. Pizarro, U. Cifuentes, N. Ramirez, and L. Djurfeldt: Subtidal dynamics in
    a deep fjord of southern Chile. Continental Shelf Research **49:** 73-89, 2012.

Castillo, M. I., U. Cifuentes, O. Pizarro, L. Djurfeldt, and M. Caceres: Seasonal hydrography
    and surface outflow in a fjord with a deep sill: the Reloncaví fjord, Chile. Ocean Sci.
    12: 533-544, 2016.

COPAS-Sur Austral: Oceanografía del fiordo Reloncaví, Universidad de Concepción,
    available at: http://www.reloncavi.udec.cl/, last access 6 June 2016, 2012.

Cossu R, Wells MG. The Interaction of Large Amplitude Internal Seiches with a Shallow
    Sloping Lakebed: Observations of Benthic Turbulence in Lake Simcoe, Ontario,
    Canada, PLOS ONE doi: 10.1371/journal.pone.0057444, 2013.

Dirección General de Aguas: Datos hidrológicos en tiempo real, Chile, available at:
    http://dgasatel.mop.cl/, last access 1 July 2016, 2016.

Djurfeldt, L.: On the response of the Fjord Gullmaren under ice cover, J. Geophys. Res., 92,
    5157-5167, doi: 10.1029/JC092iC05p05157, 1987.

Dyer, K. R.: Estuaries: A Physical Introduction, John Wiley and Sons Inc, 140 pp., UK,
    1997.

Emery, W. J., and Thomson, R. E.: Data Analysis Methods in Physical Oceanography, 634
    pp., Elsevier, New York, USA, 1998.

Farmer, D. M., and Freeland, H. J.: The physical oceanography of Fjords. Prog. Oceanogr.,
    12, 147-194, doi: 10.1016/0079-6611(83)90004-6, 1983.

Farmer, D. M., and Smith, J.: Tidal interaction of stratified flow with a sill in Knight Inlet.
    Deep-Sea Research Part A. Oceanographic Research Papers, 27, 239-254, doi:
    10.1016/0198-0149(80)90015-1, 1980.

Gill, A.: Atmosphere-Ocean Dynamics, Academics Press, 662 pp., USA, 1982.

Goudsmit, G.-H., Burchard, H., Peeters, F. and Wüest, A.: Application of k-ϵ turbulence
    models to enclosed basins: The role of internal seiches, J. Geophys. Res., 107, 3230,
    doi: 10.1029/2001JC000954, 2002.

Grinsted, A., Moore, J. C., and Jevrejeva, S.: Application of the cross wavelet transform and
    wavelet coherence to geophysical time series, Nonlin. Processes Geophys., 11, 561-
    566, doi:10.5194/npg-11-561-2004, 2004.

Inall, M. E., and. Rippeth, T. P.: Dissipation of Tidal Energy and Associated Mixing in a
    Wide Fjord, Environmental Fluid Mechanics, 2, 219-240, doi:
    10.1023/A:1019846829875, 2002.

730 Iriarte, J. L., Pantoja, S., and Daneri, G.: Oceanographic Processes in Chilean Fjords of
731   Patagonia: from small to large-scale studies, Prog. Oceanogr.,129,1-7, doi:
732   10.1016/j.pocean.2014.10.004 , 2014.
733 Large, W. G., and Pond, S.: Open-ocean momentum flux measurements in moderate to
734   strong winds, J. Phys. Oceanogr., 11, 324-336, 1981.
735 Lemmin, U.: The structure and dynamics of internal waves in Baldeggersee, Limnol.
736   Oceanogr., 32, 43-61, doi: 10.4319/lo.1987.32.1.0043, 1987.
737 León-Muñoz, J., Marcé, R., and Iriarte, J. L.: Influence of hydrological regime of an Andean
738   river on salinity, temperature and oxygen in a Patagonia fjord, Chile, New Zeal. J.
739   Mar. Fresh, 47, 515–528, doi: 10.1080/00288330.2013.802700, 2013.
740 Letelier, J., Soto-Mardones, L., Salinas, S., Osuna, P., López, D., Sepúlveda, H. H., Pinilla,
741   E., and Rodrigo, C.: Variabilidad del viento, oleaje y corrientes en la región norte de
742   los fiordos Patagónicos de Chile, Revista de Biologia Marina y Oceanografía, 46,
743   363-377. . 2011.
744 Mans, C., Bramato, S., Baquerizo, A., and Losada, M.: Surface Seiche Formation on a
745   Shallow Reservoir in Complex Terrain, J. Hydraul. Eng-Asce, 137, 517-529, 2011.
746 Maas, L. R. M., and Lam, F.-P. A.: Geometric focusing of internal waves, J. of Fluid Mech.,
747   300, 1–41, doi: 10.1017/S0022112095003582, 1995.
748 Monismith, S.: An experimental study of the upwelling response of stratified reservoirs to
749   surface shear stress, J. of Fluid Mech., 171, 407-439, doi:
750   10.1017/S0022112086001507, 1986.
751 Montero, P., Daneri, G., Gonzalez, H., Iriarte, J. L., Tapia, F.J., Lizarraga, L., Sanchez, N.,
752   and Pizarro, O.: Seasonal variability of primary production in a fjord ecosystem of
753   the Chilean Patagonia: Implications for the transfer of carbon within pelagic food
754   webs, Cont. Shelf Res., 31, 202-215, doi: 10.1016/j.csr.2010.09.003, 2011.
755 Mortimer, C. H.: Water movements in lakes during summer stratification; evidence from
756   distribution of temperature in Windermere, Phil. Trans. Roy. Soc. London, 236, 355-
757   404, doi : 10.1098/rstb.1952.0005, 1952.
758 Münnich, M., Wuest, A., and Imboden, D. M.: Observations of the 2nd Vertical-Mode of the
759   Internal Seiche in an Alpine Lake, Limnol. Oceanogr., 37, 1705-1719, doi:
760   10.4319/lo.1992.37.8.1705, 1992.
761 Niemeyer, H. & P. Cereceda.: Hidrografía. Geografía de Chile, Tomo VIII, Instituto
762   Geográfico Militar, Chile, 320 pp., 1984.
763 Palma, S., and Silva, N.: Distribution of siphonophores, chaetognaths, euphausiids and
764   oceanographic conditions in the fjords and channels of southern Chile, Deep-Sea Res.
765   Pt. II, 51, 513-53, doi:10.1016/j.dsr2.2004.05.001, 2004.
766 Pantoja, S., Iriarte, J. L., and Daneri, G.: Oceanography of the Chilean Patagonia, Cont. Shelf
767   Res., 31, 149-153, doi: 10.1016/j.csr.2010.10.013, 2011.
768 Parsmar, R., and Stigebrandt, A.: Observed damping of barotropic seiches through baroclinic
769   wave drag in the Gullmar Fjord, J. Phys. Oceanogr., 27, 849-857, 1997.
770 Pawlowicz, R.: Observations and linear analysis of sill-generated internal tides and estuarine
771   flow in Haro Strait, J. Geophys. Res-Oceans, 107, doi: 10.1029/2000JC000504, 2002.
772 Pickard, G. L.: Some Physical Oceanographic Features of Inlets of Chile, Journal of the
773   Fisheries Research Board of Canada, 28, 1077-1106, 1971.
774 Rabinovich, A.: Seiches and Harbor Oscillations, in: Handbook of Coastal and Ocean
775   Engineering, Y. Kim (ed.), World Scientific Publishing Co, United States, 193-236,
776   2010.

777   Ross L., Pérez-Santos, I., Valle-Levinson, A., Schneider, W.: Semidiurnal internal tides in a
778   Patagonian fjord, Prog. Oceanogr., 129, 19-34, doi: 10.1016/j.pocean.2014.03.006,
779   2014.
780   Schneider, W., Pérez-Santos, I., Ross, L., Bravo, L., Seguel, R. and Hernández, F.: On the
781   hydrography of Puyuhuapi Channel, Chilean Patagonia. Prog. Oceanogr., 129, 8–18,
782   doi: doi:10.1016/j.pocean.2014.03.007, 2014.
783   Simpson, J. H., Wiles P. J., and Lincoln, B. J.: Internal seiche modes and bottom boundary-
784   layer dissipation in a temperate lake from acoustic measurements, Limnol.
785   Oceanogr., 56, 1893-1906, 2011
786   Stevens, C., Imberger, J.: The initial response of a stratified lake to a surface shear stress, J.
787   of Fluid Mech., 312, 39-66, doi: 10.1017/S0022112096001917, 1996.
788   Stigebrandt, A.: Vertical diffusion driven by internal waves in a sill Fjord, J. Phys. Oceanogr.
789   6, 486-495, 1976.
790   Stigebrandt, A.: Some aspects of tidal interaction with fjord constrictions, Estuarine and
791   Coastal Marine Science, 11, 151-166, doi: 10.1016/S0302-3524(80)80038-7, 1980
792   Stigebrandt, A., and Aure, J.: Vertical Mixing in Basin Waters of Fjords, J. Phys. Oceanogr.,
793   917-926, 1989.
794   Svendsen, H.: Exchange processes above sill level between fjords and coastal water, in Fjord
795   Oceanography, H. Freeland, Farmer, D. and Levings C. (eds.), Plenum Press, USA,
796   355-361, 1980.
797   Thompson, R. O. R. Y., and Imberger J.: Response of a numerical model of a stratified lake
798   to a wind stress, in Proceedings of the 2nd International Symposium on Stratified
799   Flows, Trondheim, Norway, 24-27 June 1980, 562-570, 1980.
800   Thorpe, S.: Near-resonant forcing in a shallow two-layer fluid: a model for the internal surge
801   in Loch New?, J. of Fluid Mech., 63, 509-527, doi: 10.1017/S0022112074001753,
802   1974.
803   Torrence C., and Compo, G.P.: A practical guide to wavelet analysis, B. Am. Meteorol. Soc.,
804   79, 61-78, 1998.
805   Valle-Levinson, A., Sarkar, N., Sanay, R., Soto, D., and León, J.: Spatial structure of
806   hydrography and flow in a chilean fjord, Estuario Reloncaví, Estuaries and Coasts,
807   30, 113-126, doi: 10.1007/BF02782972, 2007.
808   Valle-Levinson, A., Blanco, J. L., and Frangópulos, M.: Depth-dependent overtides from
809   internal tide reflection in a glacial fjord, Estuaries and Coasts, 30: 127-136, 2007.
810   van der Lee E.M., and Umlauf, L.: Internal wave mixing in the Baltic Sea: Near-inertial
811   waves in the absence of tides, J. Geophys. Res-Oceans, 116, C10016, doi:
812   10.1029/2011jc007072, 2011.
813   Watson, E. R.: Movements of the waters of Loch Ness, as indicated by temperature
814   observations, The Geographical Journal, 24, 430-437, doi: 10.2307/1775951, 1904.
815   Weddernburn, E. M.: An experimental investigation of the temperature changes occurring in
816   fresh-water lochs, Proc. R. Soc. Edinb., 28, 2-20, doi: 10.1017/S0370164600011524,
817   1907.
818   Weddernburn, E. M. and Young, A.: Temperature observations in Loch Earn. Part II, Trans.
819   R. Sot. Edinb., 50, 741-767, doi: 10.1017/S0080456800017026, 1915.
820   Wiegand, R. C., and Chamberlain, V.: Internal waves of the second vertical mode in a
821   stratified lake, Limnol. Oceanogr., 32, 29-42, 1987.

822

823 **Figure captions**

824 **Figure 1:** Study region and location of the measuring stations. Left panel shows the area of

825 the Reloncavi fjord (A). The location of the Reloncavi sound (B) is also shown. The right

826 panel shows the study area (close-up view of A) and the positions of all measurements.

827 Numbers are CTD stations.

828

829 **Figure 2:** Seasonal profiles of density and bathymetry of the region. The upper panel show

830 the seasonal mean density profiles in each sub-basin of the fjord (a-d). In the panel below

831 (e.), the along-fjord bathymetry and sub-basin nomenclature are shown. The black line

832 represents the mean pycnocline depth, and corresponding standard deviations are represented

833 by the gray shading.

834

835 **Figure 3:** a) Along-fjord wind stress, positive up to the fjord, (b) sea level, (c) Puelo river

836 discharge, where the straight line represents the long-term mean. Contours of along-fjord

837 currents at (d) Cochamo, (e) Puelo and (f) the mouth; in the filled contours, the blue (red)

838 colors indicate a net outflow (inflow).

839

840 **Figure 4:** Spectra of along-fjord currents (top) at (a) the mouth, (b) Puelo and (c) Cochamo.

841 Here the black lines indicate the averaged spectra for the upper layer (depths $\leq$ h1) whereas

842 the gray lines show spectra for currents at depths > h1. (d) sea level spectra at the mouth

843 (black line) and at Cochamo (gray). (e) wind stress spectra for their along-fjord (black) and

844 cross-fjord (gray) components. At the bottom of each panel the 95% of confidence intervals

845 for 48, 24 817 and 12 degrees of freedom are shown.

846

847 **Figure 5:** The left panel shows mean density (σ_t) within the sub-basins. The panels to the

848 right of these show the first 3 baroclinic $\psi_n(z)$ modes and modal speeds obtained from the

849 CSM analysis (normalized). Note that phase velocity is in [m s^{-1}].

850

851 **Figure 6.** Band-passed along-fjord currents. Contours of band-passed (70-90 h) along-fjord

852 currents. Negative (positive) currents in blue (in red) imply an outflow (inflow). Note the

853 dotted square at the middle of August it is zooming on figure 9.

854

855   **Figure 7.** (a) Reconstruction of the along-fjord band-passed currents at the mouth using the

856   modes 1-3, (b) Band-passed along-fjord currents at the mouth, (c) Kinetic energy (K_E)

857   estimated using reconstructed currents (black), the 3 days band-pass currents (red), and the

858   diurnal and semi-diurnal band-pass currents (blue).

859

860   **Figure 8.** Coherence and phase wavelet spectra. (a) Time series of along-fjord wind stress,

861   and (b, c, d, e) coherence and phase wavelet spectra, for the relation mouth-Puelo (b, c) and

862   Puelo-Cochamo (d, e). In the contours, the thick black line indicates squared coherence $\geq$

863   0.6, only the associated phases were present on the phase wavelet. The thick black curve is

864   the influence cone for the wavelet estimations.

865

866   **Figure 9.** Time-series of along-fjord wind stress (τ) and contours of along-fjord Currents and

867   Temperatures at Cochamo, Puelo and the mouth. There are three states of wind stress based

868   on the Wedderburn number (W) with (a) strong $W< 1$, (b) weak $W> 1$ and (c) moderate $W\sim 1$

869   winds. Note that contours of the Currents and Temperature for a given location are plotted

870   together. The arrows represent the 3 days band-pass vertical velocities where the maximum

871   was 1 cm s^{-1}.

872

873   **Figure 10.** Damping signal in currents during a period of weak winds ($W>1$) at Cochamo (16

874   to 24 August 2008). The band-pass currents at 3 m depth (black line) was compared with a

875   damping oscillatory curve $x(t)= A\ e^{(-kt)}cos(\omega t +\phi\ )$ (gray line). The damping time (T_d) was

876   3.6 times longer than the fundamental internal period (T_N).

877

878

879

880

881

882

883

884 **Table titles**

885

886 **Table 1:** Characteristics of Reloncavi fjord. The name, mean depth (H) and length (L) of

887 each sub-basin and for the entire fjord are presented.

888

889 **Table 2:** Seasonal statistics of the descriptive parameters of the fjord. Here we present the
890 mean depth of the upper layer (h_1), and densities of the upper (ρ_1) and deep layers (ρ_2). In
891 addition, the phase and modal velocities (c) and theirs periods (T) estimated using the
892 Reduced Gravity and Continuously Stratified models are shown.
893

894 **Table 1.**

Sub-basin	Description	H [m]	L [km]
I	mouth–Marimeli	440	14.0
II	Marimeli – Puelo	250	13.0
III	Puelo–Cochamo	200	17.5
IV	Cochamo–head	82	10.5
Total	**mouth -head**	**250**	**55**

895

896

897

898

899

900

901

902

903

904

905

1 **Table 2.**

Reduced Gravity Model (RGM)				
h_1 [m]	ρ_1 [kg m^{-3}]	ρ_2 [kg m^{-3}]	c [m s^{-1}]	T [days]
Winter 4.60 ± 0.60	1009.72± 4.32	1024.62 ± 0.74	0.76 ± 0.01	3.37 ± 0.03
Spring 4.79 ± 0.53	1007.63± 5.32	1024.78 ± 0.62	0.87 ± 0.02	2.92 ± 0.03
Summer 4.68 ± 0.26	1008.77± 3.26	1024.78 ± 0.63	0.83 ± 0.01	3.07 ± 0.02
Autumn 4.05 ± 0.41	1009.90± 3.92	1024.95 ± 0.48	0.75 ± 0.01	3.38 ± 0.03

Continuous Stratified Model (CSM)					
c_1 [m s^{-1}]	c_2 [m s^{-1}]	c_3 [m s^{-1}]	T_1 [days]	T_2 [days]	T_3 [days]
Winter 0.73 ± 0.11	1.46 ± 0.21	2.18 ± 0.32	3.50 ± 0.25	1.75 ± 0.13	1.17 ± 0.08
Spring 0.87 ± 0.10	1.73 ± 0.21	2.59 ± 0.31	2.94 ± 0.18	1.47 ± 0.09	0.98 ± 0.06
Summer 0.84 ± 0.07	1.68 ± 0.13	2.52 ± 0.20	3.03 ± 0.12	1.51 ± 0.06	1.01 ± 0.04
Autumn 0.77 ± 0.08	1.54 ± 0.15	2.32 ± 0.23	3.30 ± 0.16	1.65 ± 0.08	1.10 ± 0.05
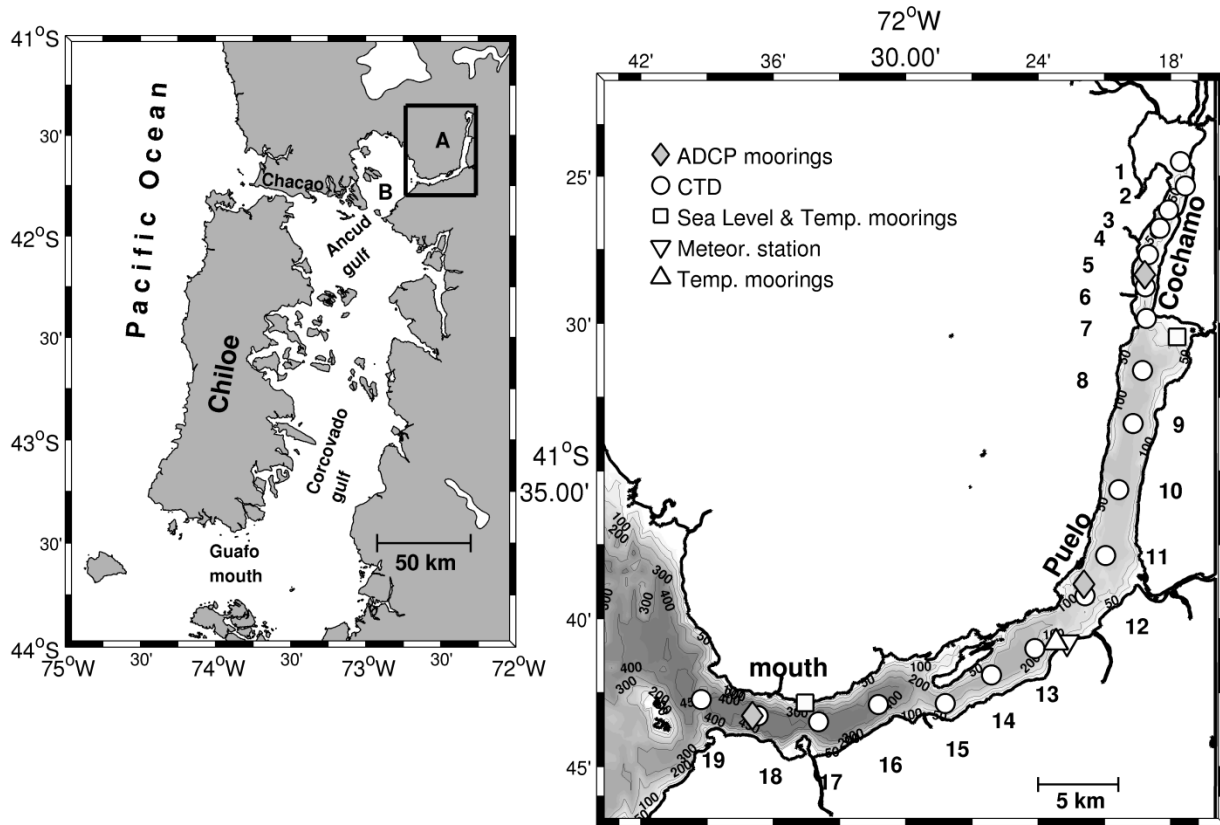
Figure 1: Study region and location of the measuring stations. Left panel shows the area of the

Reloncavi fjord (A). The location of the Reloncavi sound (B) is also shown. The right panel

shows the study area (close-up view of A) and the positions of all measurements. Numbers are

CTD stations.
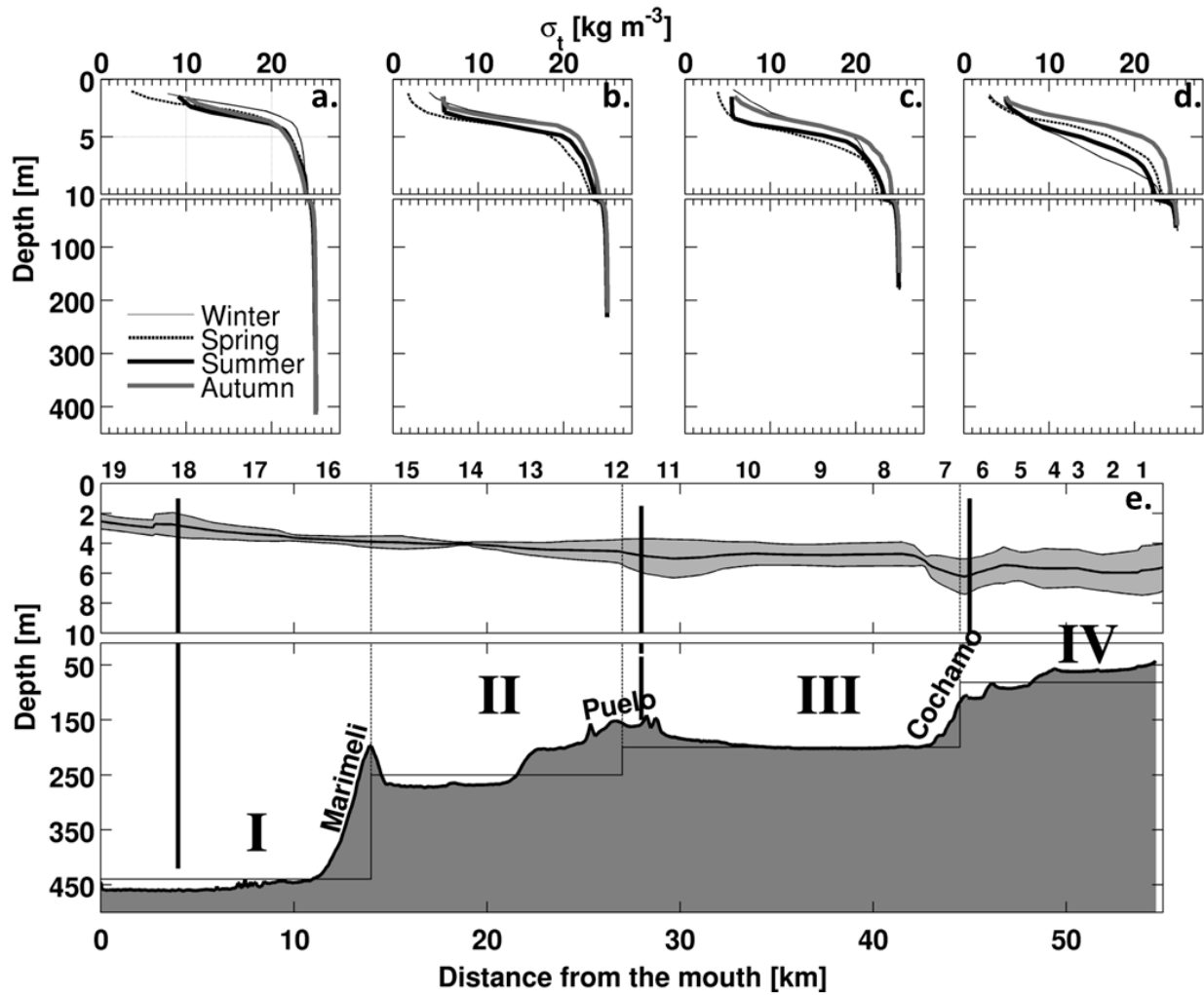
Figure 2: Seasonal profiles of density and bathymetry of the region. The upper panel show the seasonal mean density profiles in each sub-basin of the fjord (a-d). In the panel below (e.), the along-fjord bathymetry and sub-basin nomenclature are shown. The black line represents the mean pycnocline depth, and corresponding standard deviations are represented by the gray shading.
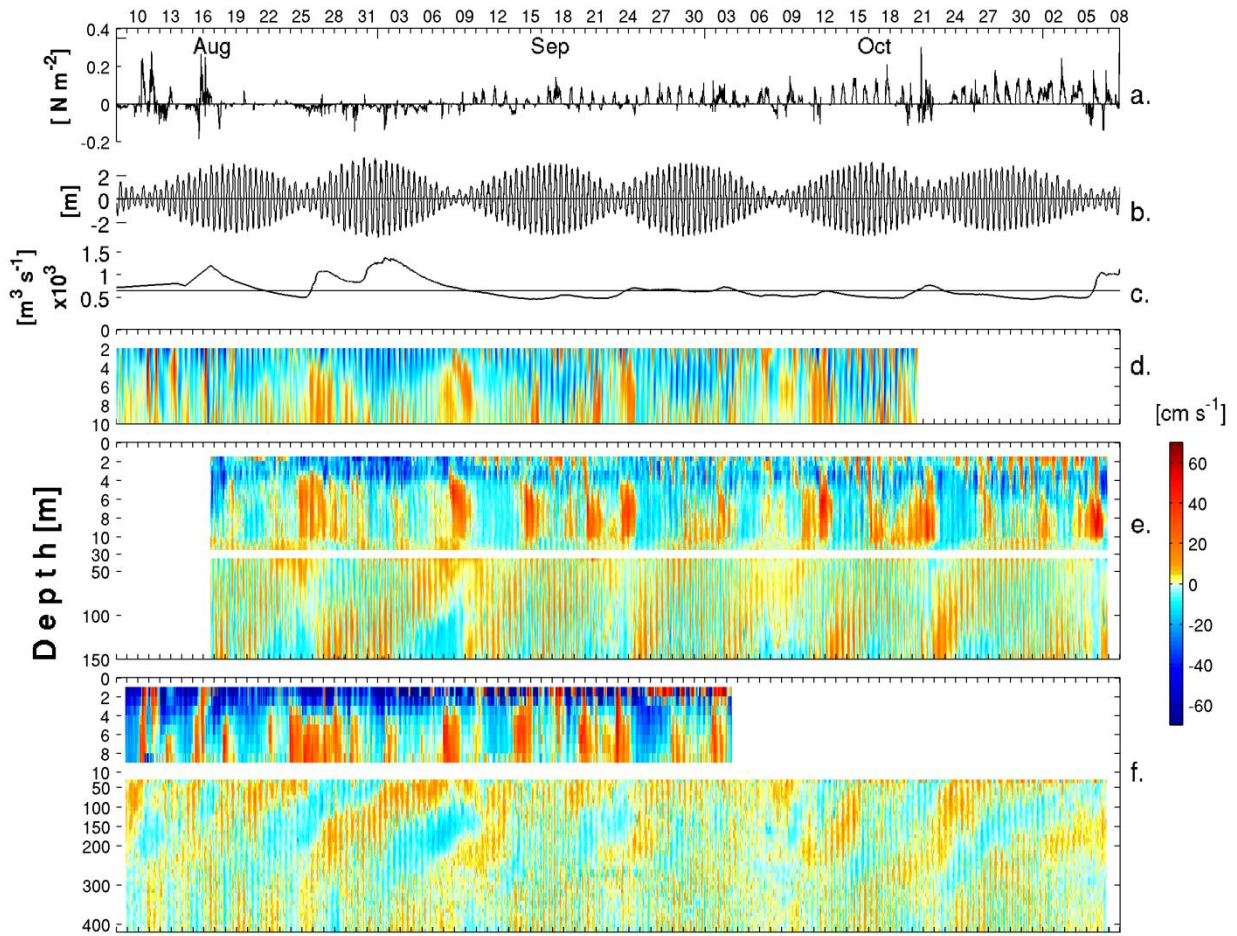
Figure 3: a) Along-fjord wind stress, positive up to the fjord, (b) sea level, (c) Puelo river
discharge, where the straight line represents the long-term mean. Contours of along-fjord currents
at (d) Cochamo, (e) Puelo and (f) the mouth; in the filled contours, the blue (red) colors indicate a
net outflow (inflow).
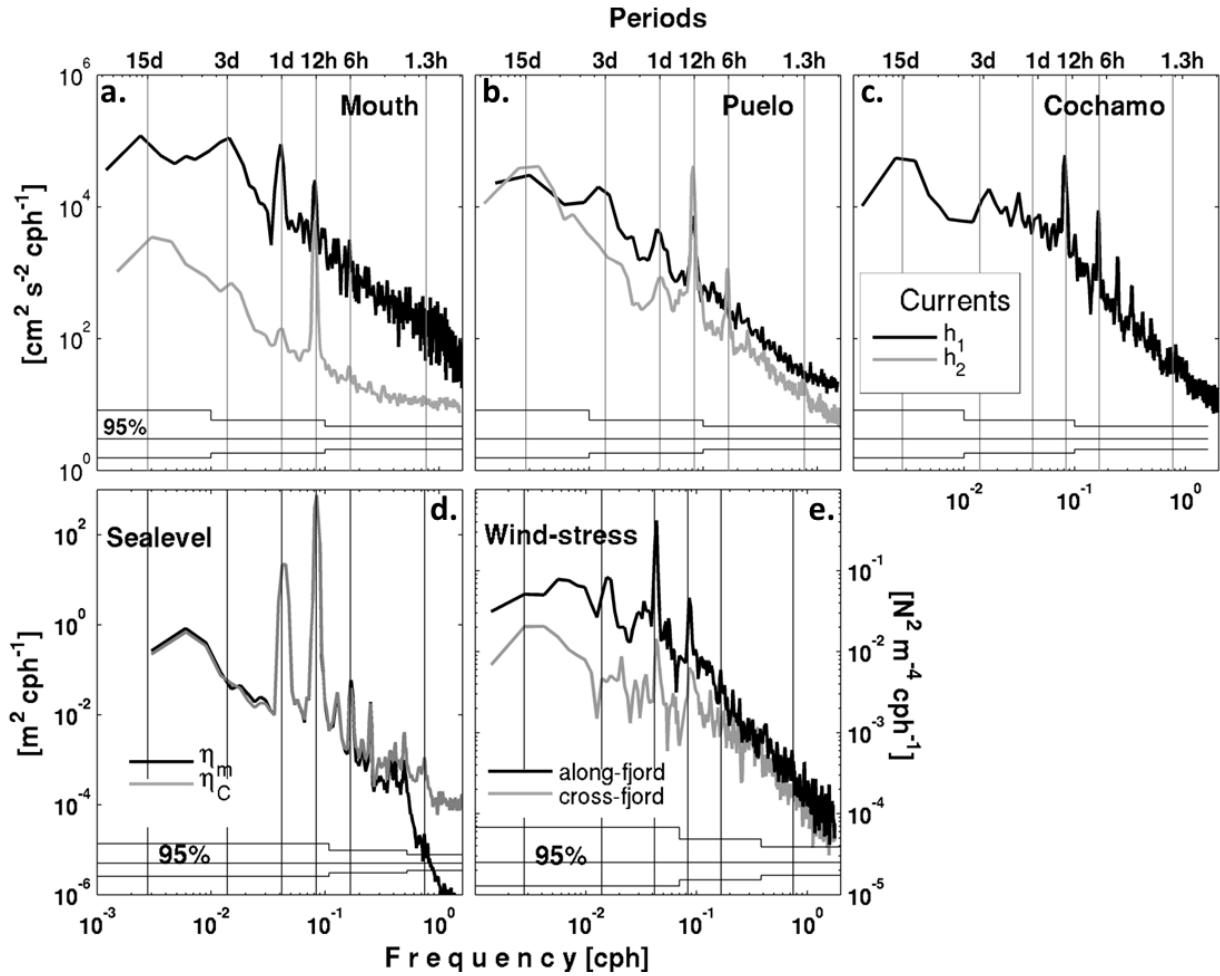
Figure 4: Spectra of along-fjord currents (top) at (a) the mouth, (b) Puelo and (c) Cochamo. Here the black lines indicate the averaged spectra for the upper layer (depths $\leq h1$) whereas the gray lines show spectra for currents at depths $> h1$. (d) sea level spectra at the mouth (black line) and at Cochamo (gray). (e) wind stress spectra for their along-fjord (black) and cross-fjord (gray) components. At the bottom of each panel the 95% of confidence intervals for 48, 24 817 and 12 degrees of freedom are shown.
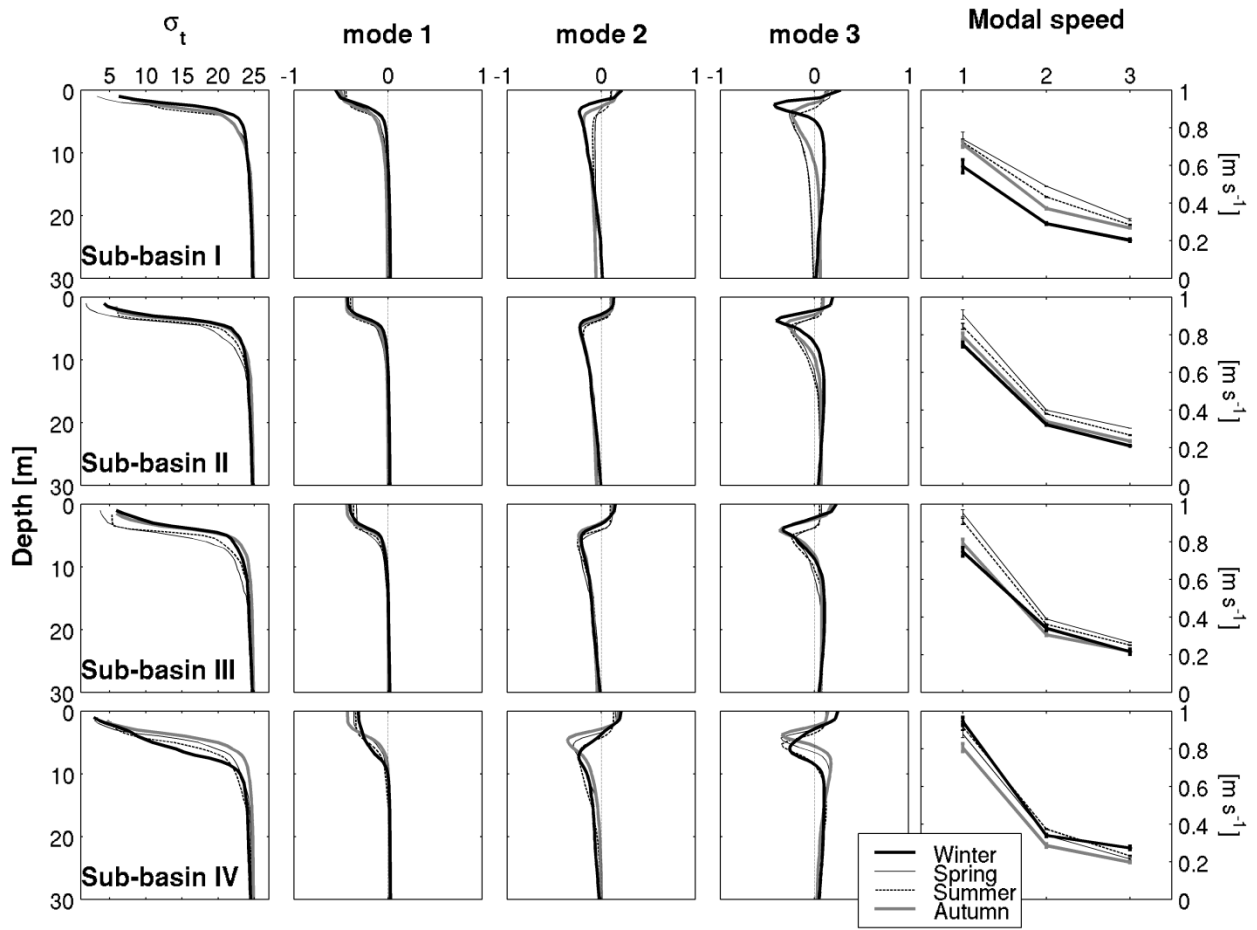
3 **Figure 5:** The left panel shows mean density (σ_t) within the sub-basins. The panels to the right of

4 these show the first 3 baroclinic $\psi_n(z)$ modes and modal speeds obtained from the CSM analysis

5 (normalized). Note that phase velocity is in [m s^{-1}].
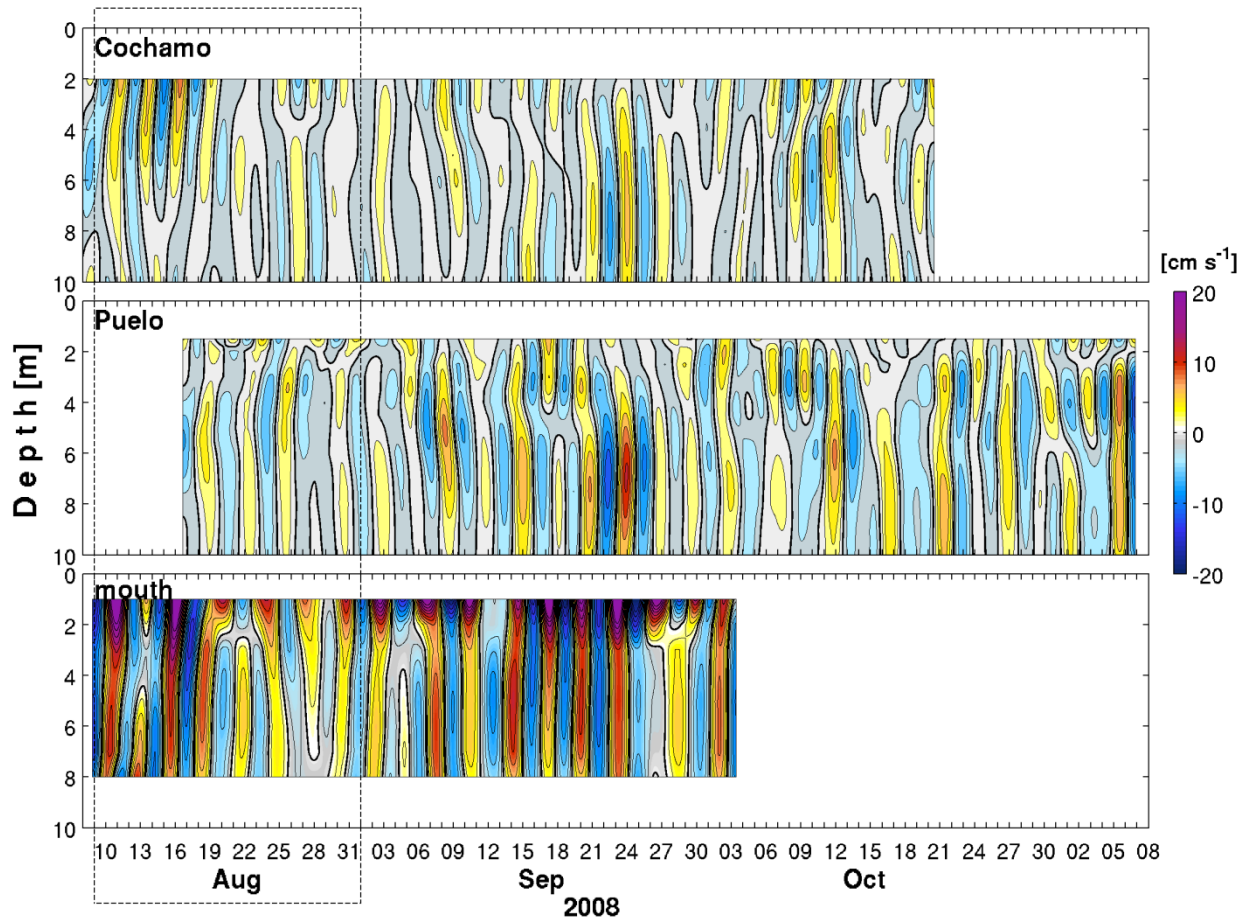
Figure 6. Band-passed along-fjord currents. Contours of band-passed (70-90 h) along-fjord

currents. Negative (positive) currents in blue (in red) imply an outflow (inflow). Note the dotted
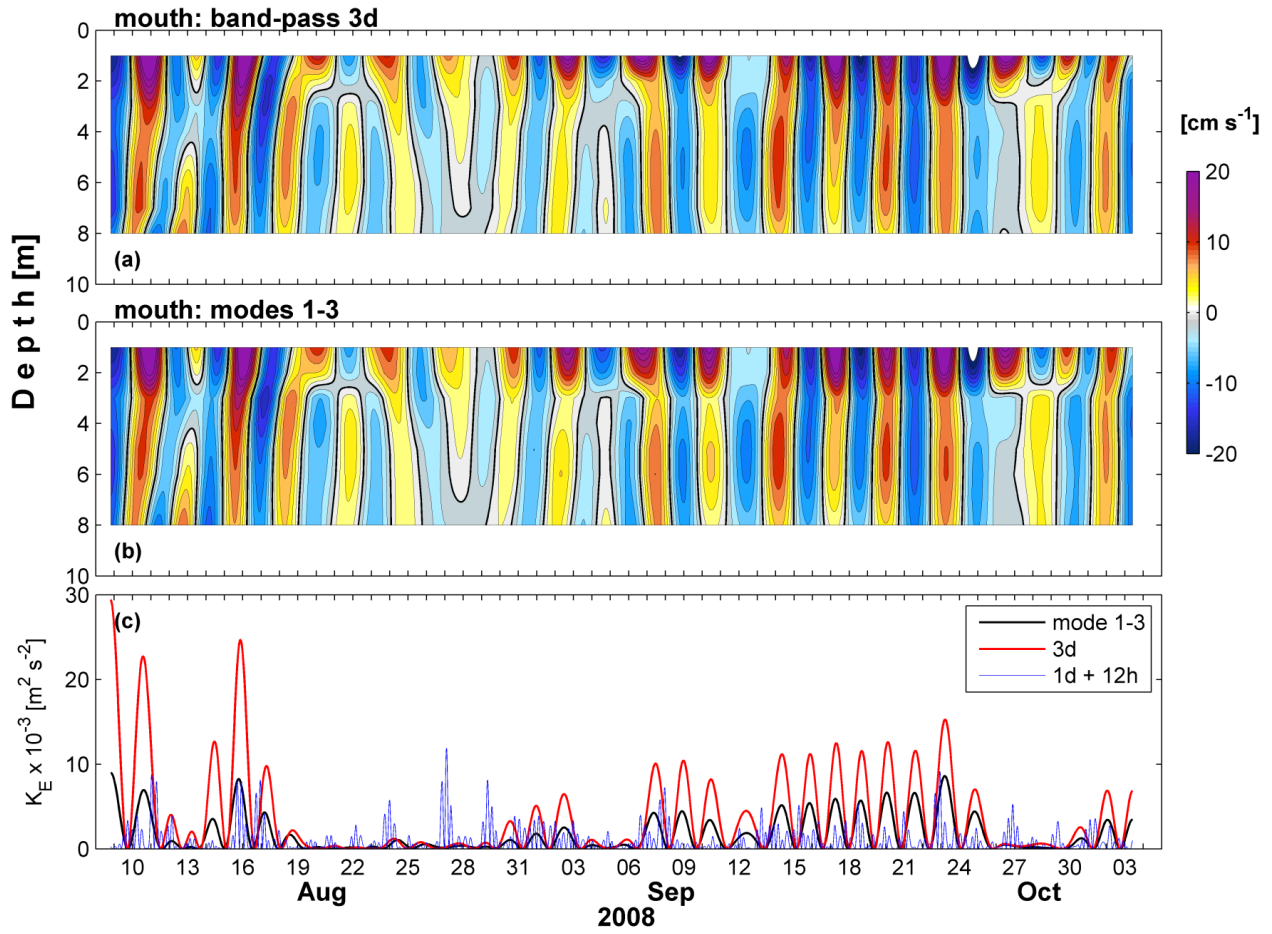
square at the middle of August it is zooming on figure 9.

Figure 7. (a) Reconstruction of the along-fjord band-passed currents at the mouth using the

modes 1-3, (b) Band-passed along-fjord currents at the mouth, (c) Kinetic energy (K_E) estimated

using reconstructed currents (black), the 3 days band-pass currents (red), and the diurnal and

semi-diurnal band-pass currents (blue).
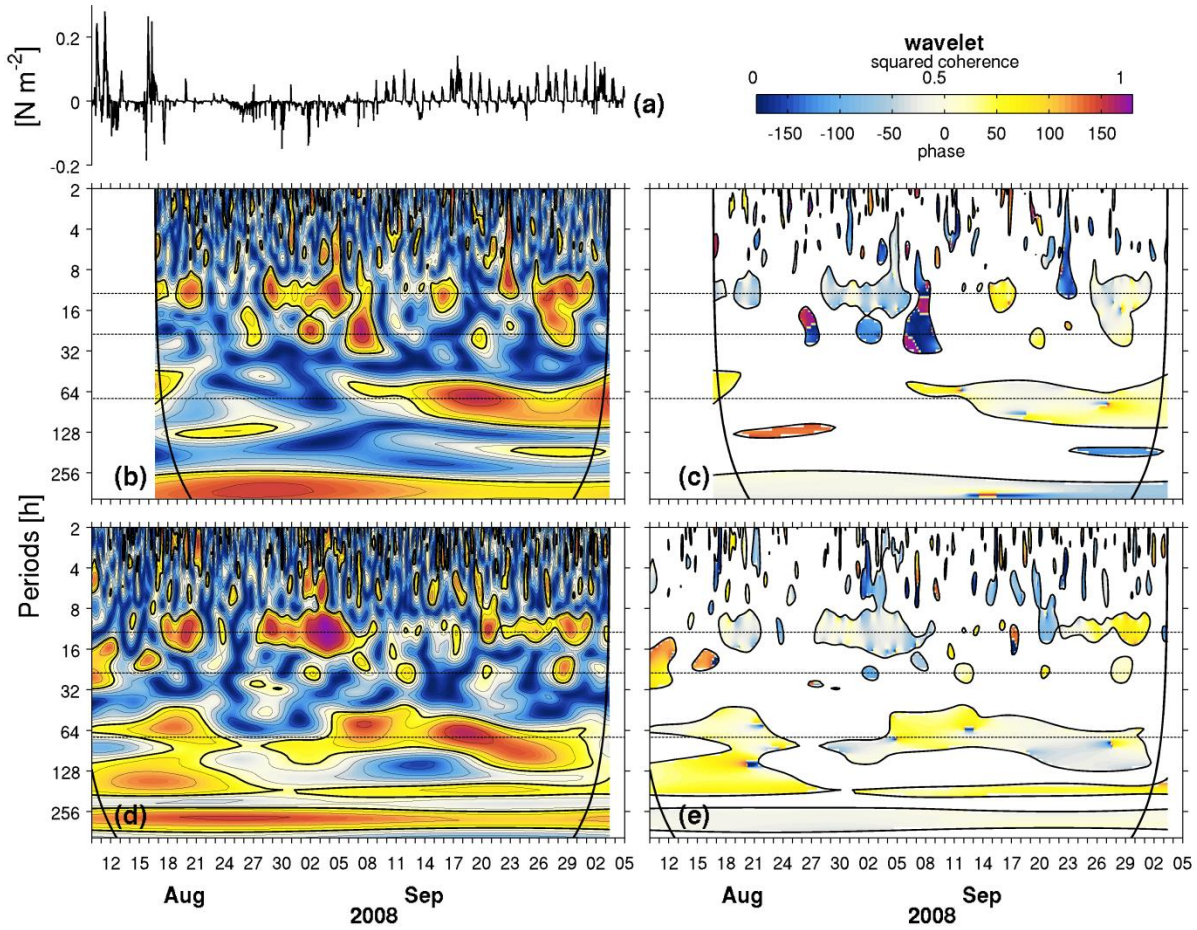
Figure 8. Coherence and phase wavelet spectra. (a) Time series of along-fjord wind stress, and (b, c, d, e) coherence and phase wavelet spectra, for the relation mouth-Puelo (b, c) and Puelo-Cochamo (d, e). In the contours, the thick black line indicates squared coherence ≥ 0.6, only the associated phases were present on the phase wavelet. The thick black curve is the influence cone for the wavelet estimations.
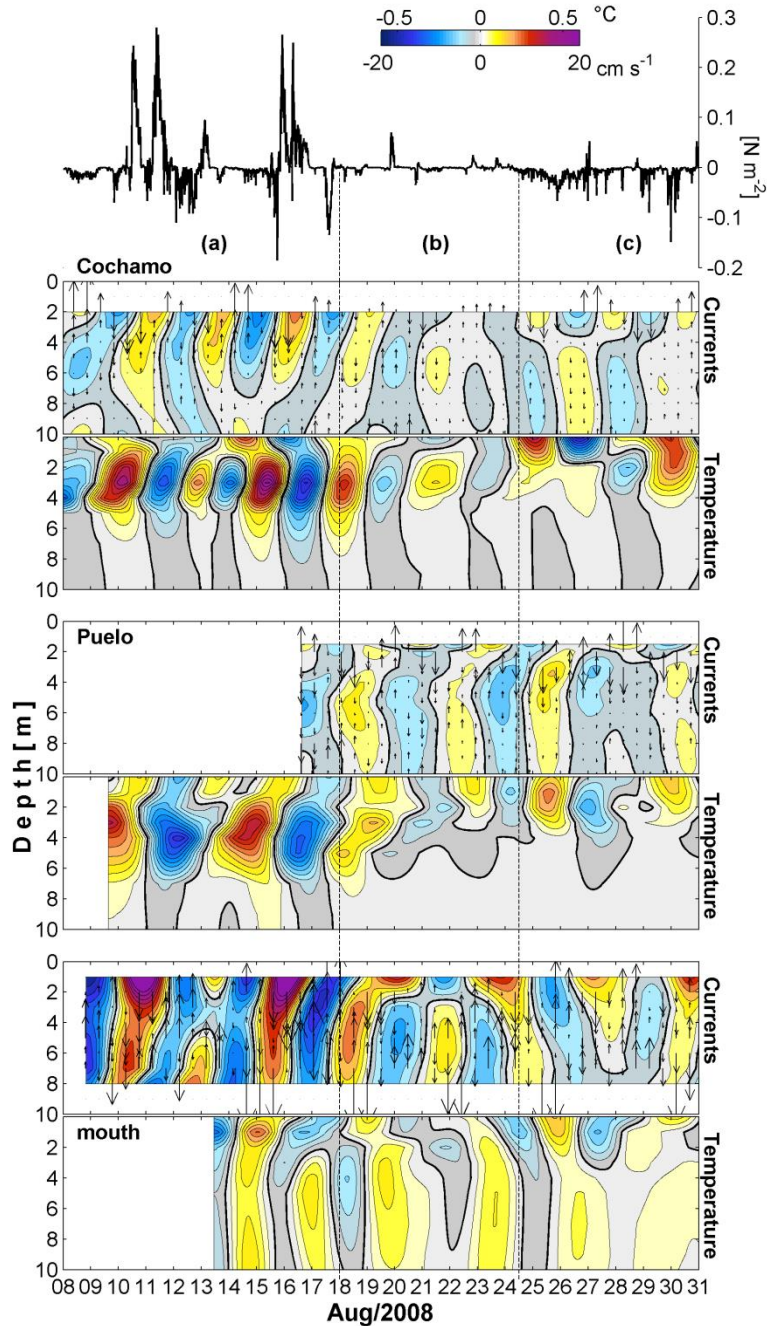
2 **Figure 9.** Time-series of along-fjord wind stress (τ) and contours of along-fjord Currents and

3 Temperatures at Cochamo, Puelo and the mouth. There are three states of wind stress based on

4 the Wedderburn number (*W*) with (a) strong *W*< 1, (b) weak *W*> 1 and (c) moderate *W*~ 1 winds.

5 Note that contours of the Currents and Temperature for a given location are plotted together. The

6 arrows represent the 3 days band-pass vertical velocities where the maximum was 1 cm s^{-1}.
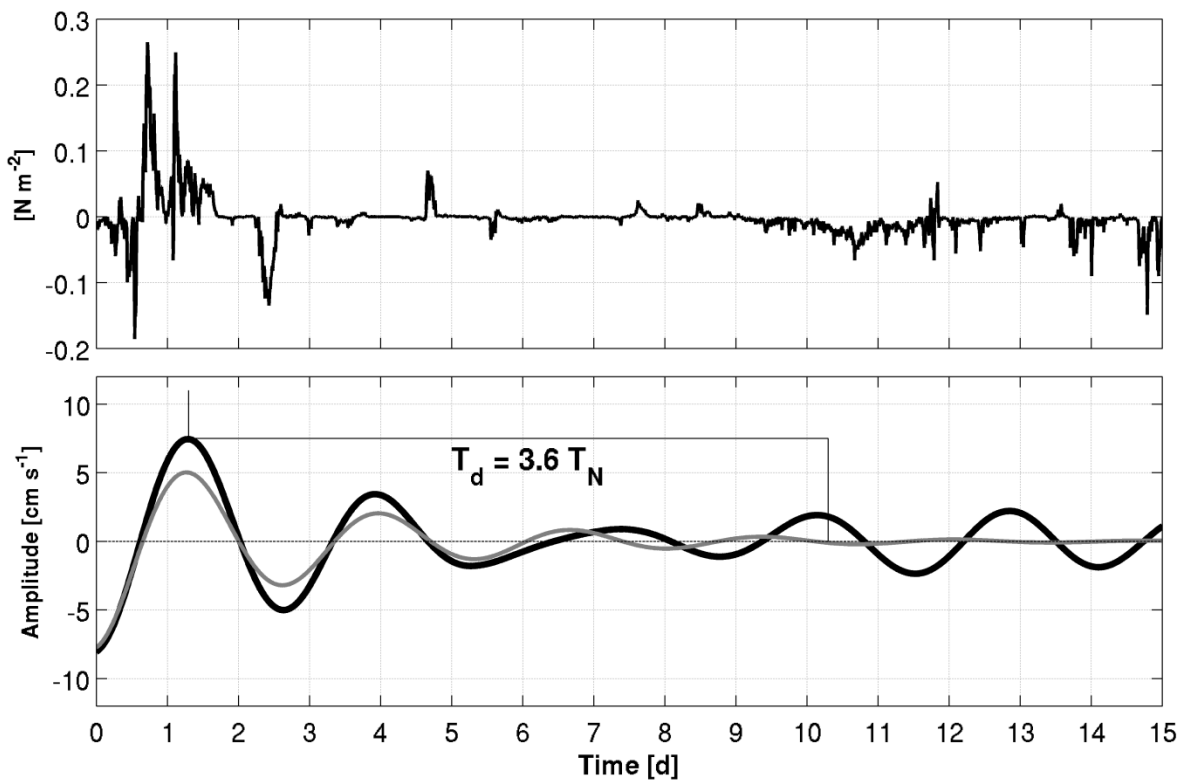
Figure 10. Damping signal in currents during a period of weak winds ($W>1$) at Cochamo (16 to
24 August 2008). The band-pass currents at 3 m depth (black line) was compared with a damping
oscillatory curve $x(t)= A\ e^{(-kt)}cos(\omega t + \phi\ )$ (gray line). The damping time (T_d) was 3.6 times longer
than the fundamental internal period (T_N).